Impact of urban environment on Savonius wind turbine performance: A numerical perspective

6 authors, including:

Riccardo Longo
Université Libre de Bruxelles
12 PUBLICATIONS **140** CITATIONS

SEE PROFILE

Matteo Natalini
BlueThink SpA
1 PUBLICATION **16** CITATIONS

SEE PROFILE

Paolo Schito
Politecnico di Milano
84 PUBLICATIONS **658** CITATIONS

SEE PROFILE

Riccardo Mereu
Politecnico di Milano
63 PUBLICATIONS **1,319** CITATIONS

SEE PROFILE

Some of the authors of this publication are also working on these related projects:

Project   A new comprehensive K-Omega model View project

Project   IMPARAR - Improving access to resources at reduced risk for urban areas with informal settlements: towards sustainable growth for Guayaquil View project

Impact of urban environment on Savonius wind turbine performance: a numerical perspective

Riccardo Longo[*][b,a], Patricia Nicastro[c], Matteo Natalini[c], Paolo Schito[d], Riccardo Mereu[c], Alessandro Parente[a,e]

[a]*Université Libre de Bruxelles - Aéro-Thermo-Mécanique Department*
[b]*Politecnico di Milano - Dipartimento di Chimica, Materiali ed Ingegneria Chimica "G. Natta"*
[c]*Politecnico di Milano - Dipartimento di Energia*
[d]*Politecnico di Milano - Dipartimento di Meccanica*
[e]*Combustion and Robust Optimization Group (BURN), Université libre de Bruxelles and Vrjie Universiteit Brussel, Bruxelles, Belgium*

Abstract

In this study, computational fluid dynamics (CFD) is employed to evaluate the influence of surrounding buildings on the performance of a roof-mounted, 2-bladed Savonius vertical-axis wind turbine (VAWT). The latter is planned to be located in the Bovisa Campus of Politecnico di Milano. In the present work a preliminary simulation campaign has been conducted, explicitly depicting the surrounding area and employing an advanced Reynolds-averaged Navier-Stokes (RANS) model. This closure is suitable for Atmospheric Boundary Layer (ABL) simulation, reliably reproducing the various ground roughness elements and employing a Building Influence Area (BIA) for a more accurate representation of the disturbed flowfield. After considering twelve main wind directions, the resulting velocity profiles are extracted and used as inlet conditions for a second session of simulations, related to the wind turbine.

The final goal is to reproduce the effect of the surrounding buildings and to accurately forecast the energy production of the machine. This is a relevant aspect of the increasingly topical framework of smart city, implying the exploitation of wind energy. Outcomes indicate that the resulting energy production of the machine remarkably departs from ideal conditions and that accounting for the surrounding topography becomes an aspect of great relevance.

[*]Corresponding authors' emails: riccardo.longo@ulb.ac.be
[**]Present address: Av. F.D. Roosevelt 50, 1050 Bruxelles-Belgique
Declarations of interest: none

Keywords

Urban wind energy generation; Renewable Energy; Vertical-axis wind turbine; Atmospheric boundary Layer; Computational Fluid Dynamics; Sustainable built environment.

Nomenclature

Symbol	Description
A_x	BIA attenuation parameter
C_1, C_2	constant in the k inlet profile
$C_\mu, C_{\epsilon 1}, C_{\epsilon 2}, \sigma_\epsilon$	constants in the $k - \epsilon$ model
C_m, C_d, C_l, C_p	torque, drag, lift and power coefficient for wind turbine
E	annual energy yield, J
F_S	safety factor
f_c	Coriolis parameter, rad/s
f_i	relative frequency during the year
h	ABL height, m
H_n, H_{max}	building's heights, m
k	turbulent kinetic energy, $m^2 s^{-2}$
p	pressure, $N m^{-2}$
p_c	order of convergence
P_{avail}	available power, W
r_h	coarsening ratio
S	strain-rate invariant
S_ϵ	source term in the ϵ equation
$\vec{u}$	wind velocity vector, $m\ s^{-1}$
U	mean streamwise wind speed, $m\ s^{-1}$
U_p	wind speed at first cell centroid, $m\ s^{-1}$
U_{ref}	reference wind speed, $m\ s^{-1}$
U_{inf}	reference wind turbine speed, $m\ s^{-1}$
u_*	ABL friction velocity, $m\ s^{-1}$

x, y, z	stream-wise, width and height coordinates, m
$\widetilde{y}^+, y^+$	non-dimensional wall distances
z_0	aerodynamic roughness length, m
$\delta_u, \delta_k, \delta_\epsilon, \delta_h$	local deviation of turbulent properties
δ_*	deviation in the sinusoidal simulation
ϵ	turbulent dissipation rate, $m^2 s^{-3}$
κ	von Karman constant
μ_t	dynamic turbulent viscosity, $kg\ m^{-1} s^{-1}$
ω	specific rate of dissipation, s^{-1}
Ω	vorticity invariant
ρ	density, $kg\ m^{-3}$

1. Introduction

Energy sector researches and investments are more and more focused on renewable energy, in a framework where decentralization is playing an important role [1, 2, 3, 4, 5]. In this scenario, small wind turbines are one of the most promising solutions [6]; currently, Savonius vertical-axis wind turbines (VAWT) are still not widespread, but their simplicity and better performance in disturbed flowfields, compared to small horizontal-axis wind turbines (HAWT) make them a good alternative for distributed generation devices in urban environment [7, 8].

CFD can be succesfully employed to provide detailed information on the urban flowfield [9, 10]. In this regard, Reynolds-averaged Navier–Stokes two-equation models can still offer a good compromise between accuracy of results and computational time [11, 12, 13]. However, when applied with the standard wall treatment, the conventional Richard and Hoxey [14] inlet profiles suffer from horizontal inhomogeneity [15, 16, 17]. One of the reasons for the decay of the turbulence profiles lies in the inconsistency between the fully developed inlet profiles and the rough wall formulation [16, 18, 19]. Moreover, buildings introduce swirl and recirculation zones that are not accurately reproduced by the standard two-equation models [20, 21, 16, 17, 22].

To address these issues and to reproduce more realistic inlet conditions at a reasonable computational cost, this study employs the comprehensive approach [23, 18, 16]. This model was designed for undisturbed flowfield, aiming to employ realistic inlet conditions and to solve the inconsistencies related to neutral

atmospheric boundary layer (ABL); it was developed together with a wall treatment which is consistent with the model's equations [18].

Further advances are needed to extend the turbulence treatment to the case of disturbed flowfields: Longo et al. [16, 17] employed different Non-Linear Eddy-Viscosity (NLEV) models inside an automatically detected Building Influence Area (BIA), outperforming the standard RANS two equations models, with enhanced sensitivity to curvature, swirl and recirculation zones [21, 16, 22, 21, 20]. In the present work, all the aforementioned turbulence improvements have been implemented in OpenFOAM®. Moreover, a new concept of BIA is introduced to accurately detect the disturbance produced by the presence of buildings. The resulting turbulence model is validated over three wind tunnel test cases and one real-scale case, provided with experimental data. Subsequently, it is employed on the Bovisa Campus, considering twelve wind directions.

The resulting flow pattern will aerodynamically characterize the location selected for the wind turbine. The subsequent step will be the coupling between the ABL simulations on the Bovisa Campus and the wind turbine simulations. The turbulence conditions in the target location will be extrapolated and employed as inlet conditions for the wind turbine simulation.

Literature about Savonius VAWT studies includes both wind tunnel tests and numerical simulations. Typically, the first ones are mostly focused on the optimization of the blade shape [24] and consist in wind tunnel test measurements [25] at different tip-speed ratio (TSR), overlap ratios and aspect ratios or even multiple stage designs [26, 27]). In this regard, CFD studies can be mainly classified considering 2D and 3D inspection methods. 3D methods are preferable, being more consistent with experimental results [28, 29, 30]; the majority of those studies consists in validation processes for different RANS turbulence models, among which the Shear Stress Transport $k - \omega$ (SST $k - \omega$) is one of the most reliable.

One of the main obstacles to the deployment of this technology is the gap between the forecast and actual energy production. This can be related to the fact that real operating conditions are frequently not considered: these are affected by the surrounding environment [31, 32, 33] which, in the case of urban context, is strongly case-dependent.

In the last decades, few studies concerning building interactions with wind turbines have been carried out, considering simplified building models [34] and neglecting the neighbour building's influence on wind stream [35]. In the present work, the built environment around the target building is explicitly depicted and a turbulence model accounting for the main ABL features is employed to represent the local flowfield and realistically forecast the operating conditions of the machine. The results indicate that the location selected

on the target building is suitable for wind energy exploitation and that surrounding environment is playing a

non-negligible role on the efficiency of the wind turbine energy production. Conducting the same analysis

with the ideal inlet conditions would have led to a severe misprediction of the energy production of the

machine.

2. ABL turbulence modelling

Considering its feasibility and robustness, the $k - \epsilon$ model remains one of the most common RANS closures for ABL simulations [36, 37, 38, 39, 40]. However, when applied in its standard form, it suffers from several drawbacks: overprediction of turbulent kinetic energy in stagnation regions, mis-representation of recirculation zones and insensitivity of shear stress to the curvature [21, 41, 42, 43]. Moreover, a rise of stream-wise gradients in the vertical profiles of turbulent quantities is generally observed if the inlet conditions are not properly selected and they are not consistent with the wall treatment [17, 19]. For these reasons, an advanced/consistent ABL $k - \epsilon$ model, validated in a number of studies [44, 23, 18, 16, 45, 46], is employed, guaranteeing the reduction of the horizontal inhomogeneity in the inlet profiles, addressing the problem of erroneous representation of disturbed flow regions and properly treating the various roughness elements.

2.1. Undisturbed and disturbed flowfield treatment

The comprehensive approach [23, 18, 16] is a turbulence model suitable for undisturbed flowfield. It consists in the combination of appropriate boundary conditions, fulfilling ABL experimental data evidence and consistent with the wall treatment (Table 1).

Table 1: Set of inlet conditions and turbulence variables for the comprehensive approach [17].

Inlet Conditions	Turbulence Model
$U = \frac{u_*}{\kappa} ln\left(\frac{z+z_0}{z_0}\right)$	$\mu_t = C_\mu \rho \frac{k^2}{\epsilon}$
$k\left(z\right) = C_1 ln\left(z + z_0\right) + C_2$	$S_\epsilon\left(z\right) = \frac{\rho u_*^4}{(z+z_0)^2}\left(\frac{(C_{\epsilon 2} - C_{\epsilon 1})\sqrt{C_\mu}}{\kappa^2} - \frac{1}{\sigma_\epsilon}\right)$
$\epsilon\left(z\right) = \frac{u_*^3}{\kappa(z+z_0)}$	$C_\mu = \frac{u_*^4}{k^2}$

When dealing with disturbed flowfields a different modelling strategy has to be considered [16]. In this regard, one possible solution is represented by NLEV models [21, 20, 22] which can accurately catch the streamline curvature and swirl of a perturbed flowfield, thanks to the inclusion of quadratic and cubic terms

99   to the stress-strain relation and to the employment of a C_μ depending on the local strain-rate and vorticity

100 invariants. The NLEV model selected for this study is the one proposed by Ehrhard and Moussiopoulos

101 [22], which defines C_μ as:

$$C_\mu = min \left[\frac{1}{0.9S^{1.4} + 0.4\Omega^{1.4} + 3.5}, 0.15 \right] \tag{1}$$

102

103 The NLEV model is automatically employed whenever a disturbed flowfield is detected, through the adop-

104 tion of a Building Influence Area [23, 17, 16]. The BIA is identified using a local deviation parameter δ that

105 estimates the relative error between homogeneous ABL conditions and the local values of relevant turbu-

106 lence parameters.

107 In this work, the BIA concept is further improved, combining three different deviations in the so-called hybrid

108 BIA. More precisely, the maximum of three local deviations ($u - k - \epsilon$) is assigned to the cell and defines

109 the hybrid blending parameter δ_h, which reads:

$$\delta_h = max \left[\delta_u, \delta_k, \delta_\epsilon \right] \tag{2}$$

110 For a generic turbulent variable x, the deviation reads:

$$\delta_x = min \left[A_x \left| \frac{x_{wake} - x_{ABL}}{x_{ABL}} \right|, 1 \right] \tag{3}$$

111 A_x is an attenuation parameter, meant to limit the unnecessary over-extent of the BIA. Turbulent kinetic

112 energy and turbulent dissipation rate are, by nature, more abrupt and scattering quantities, compared

113 to velocity. Their variability affects, consequently, the respective relative deviation. For this reason, the

114 attenuation parameters recursively employed are: $A_u = 1$, $A_k = 0.1$ and $A_\epsilon = 0.1$. Their calibration was

115 succesfully validated on the basis of different wind tunnel and real scale test cases (some of them are

116 located in the supplementary material), all provided with experimental data [17, 47, 48, 45, 46]; x_{wake} is

117 the local turbulence parameter value, x_{ABL} is the undisturbed value. If the flowfield is undisturbed, the

118 resulting deviation is zero: $\delta_x = 0$. On the contrary, a fully perturbed region would bring to a maximum

119 deviation: $\delta_x = 1$. The behavior of the blending approaches is explained in Table 2, where the BIA extent

120 is shown for four primitive geometries. These are the building blocks for many other shapes/forms. The

121 deviation δ_h is then used to blend the comprehensive approach and the NLEV model parameters between

122 the undisturbed ABL and the BIA through a proper transition function [23, 49].

6

123 Further information about the BIA metrics and the turbulent model employed in this study can be found in

124 [23, 16] and in the supplementary material.

125 Similarly to Montazeri et al. [50], Longo et al. [16] compared the ABL model against a number of other

126 RANS approaches, proving the enhancement in accuracy of the proposed approach with respect to different

127 turbulence methodologies.
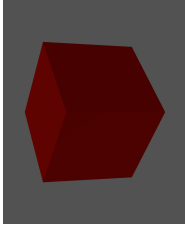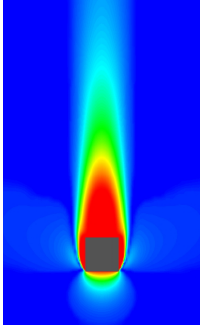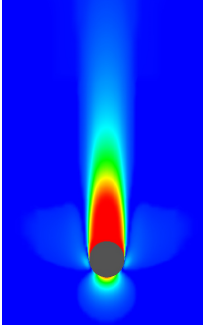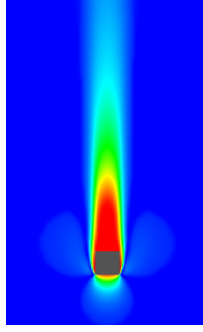
Building Influence Area
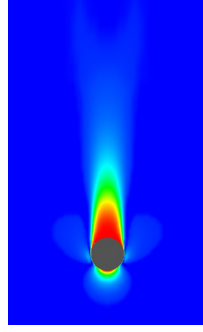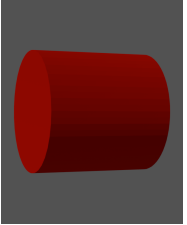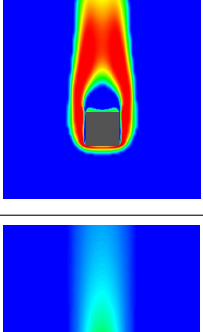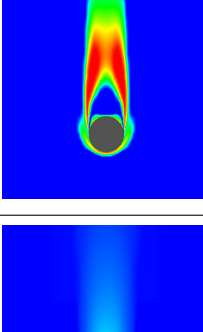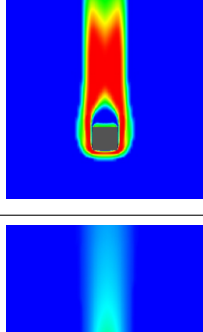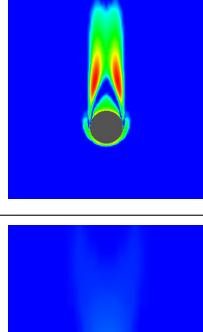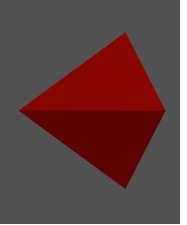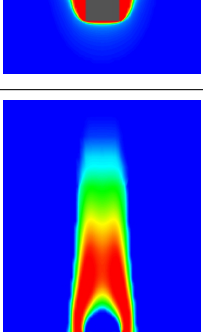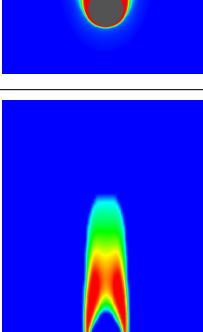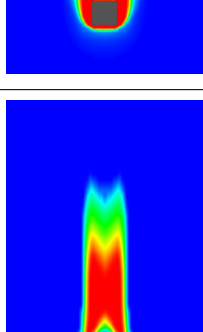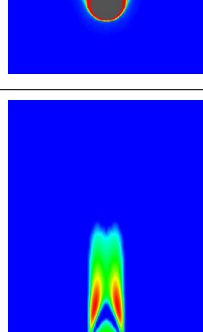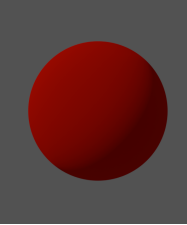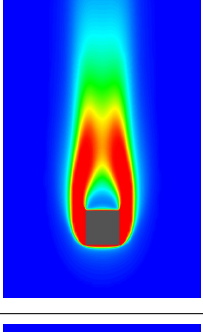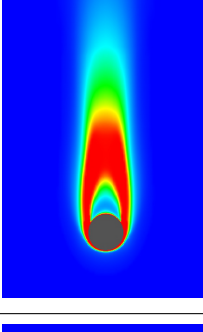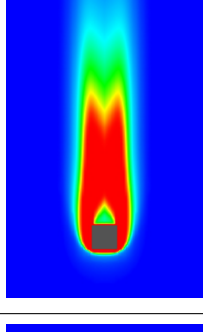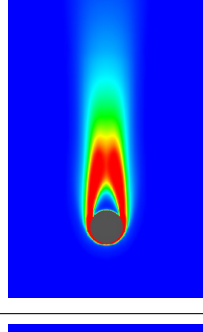
Solid Primitives	Pure BIA			Hybrid BIA
	$\delta_u = min\left[A_u\left|\frac{u-u_{ABL}}{u_{ABL}}\right|,1\right]$	$\delta_k = min\left[A_k\left|\frac{k-k_{ABL}}{k_{ABL}}\right|,1\right]$	$\delta_\epsilon = min\left[A_\epsilon\left|\frac{\epsilon-\epsilon_{ABL}}{\epsilon_{ABL}}\right|,1\right]$	$\delta_h = max[\delta_u,\delta_k,\delta_\epsilon]$

Table 2: Metric and extent of the BIA for the pure blending, based on the local deviation of u, k and ϵ, and hybrid blending, displayed on the horizontal plane for four primitive shapes: cube, cylinder, pyramid and sphere. The blue color represents a completely undisturbed flowfield, while the red one indicates a completely perturbed one. For all the geometries, the BIA metrics differently identify the disturbed areas and their combination in the Hybrid BIA results in the most exhaustive detection.

2.2. Validation of the ABL turbulence model

129 The Case B displays a 4:4:1 shaped building from the wind tunnel tests performed by Tominaga et al. [51],

130 displayed in Figure 1. The proposed ABL approach and the standard $k - \epsilon$ model are compared against
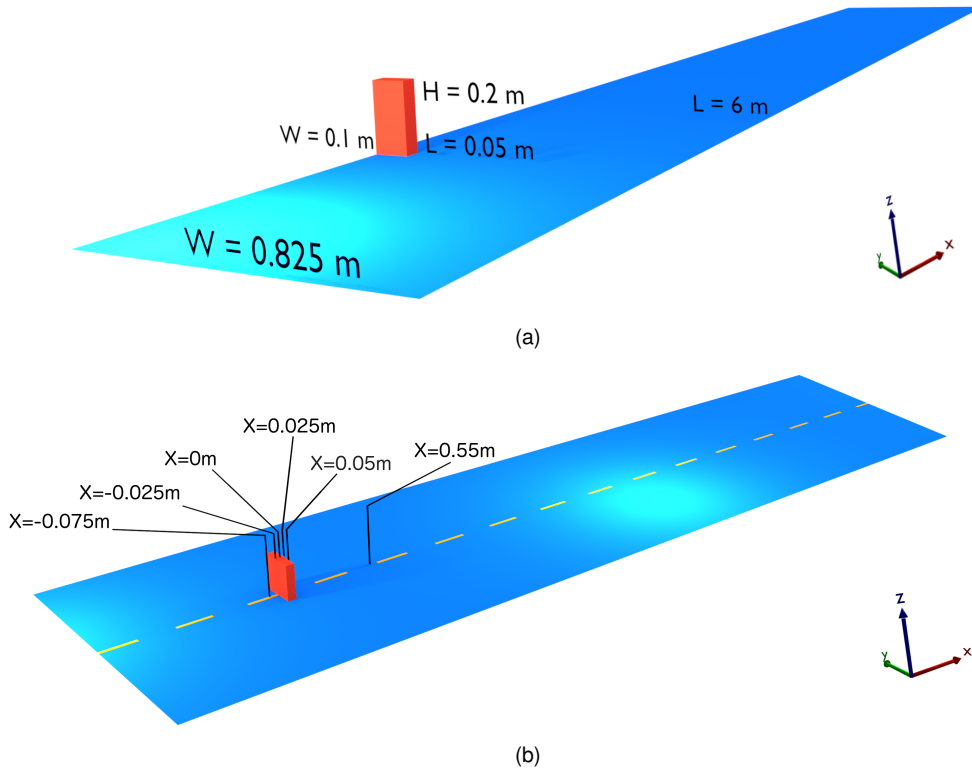
the experimental data.

(a)

(b)

Figure 1: View, geometry (a) and vertical measurement lines (b) of the Case B from the Architectural Institute of Japan [51].

131
132 A mesh of 2 millions cells (330x78x78 hexa elements) was generated. Considering the symmetry of the

133 model with respect to the plane $y = 0m$, only half of the domain was studied, resulting in: length $L = 6m$,

134 width $W = 0.825m$ and height $H = 1.6m$. As shown in Figure 2, the mesh is finer close to the building and

135 to the ground boundaries, gradually decreasing in resolution once moving away from the region of interest.

136 As for the dimensionless wall distance, its values ranged between 50 and 190 all over the domain. A grid

137 sensitivity analysis was carried out, building one finer grid, consisting of 3.2 million cells ($r_h = 1.18$), with a

138 resulting y^+ ranging between 40 and 155. A conservative safety factor, $F_S = 3$, was employed. A GCI of

139 2% was determined both for u and k, with respect to the finest grid.

140 The roughness lenght z_0 is equal to $0.000096m$. From Figures 3, it is possible to observe that the velocity

141 prediction is improved applying the ABL approach. This can be witnessed in Figure 3 (a-b-c-d), where the

<div align="center">(a)   (b)</div>
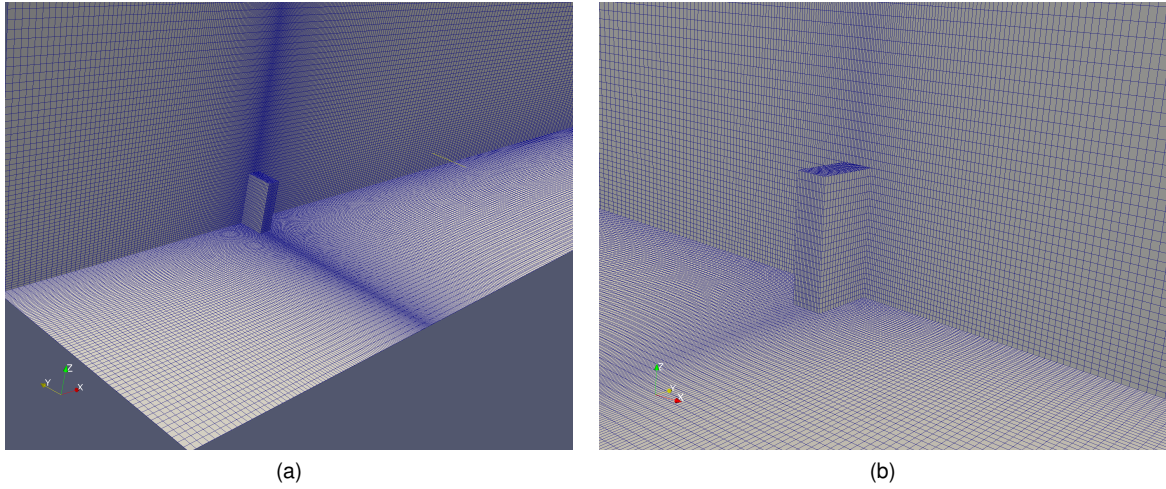
Figure 2: Computational mesh on the building, ground and symmetry surfaces for the Case B, from upwind (a) and donwnwind (b) views

.

upwind recirculation zone and the separation bubble above the building are better reproduced.

As for k, its overproduction is reduced by the employment of the BIA. This is evident when considering

Figure 4, especially at the impinging side of the building, with the standard $k - \epsilon$ over-predicting turbulent

kinetic energy up to 500%.

Figure 3: Comparison of experimental and numerical predictions of x-velocity for the Case B test case [51] at different locations of the domain, employing the standard $k - \epsilon$ model and the proposed ABL turbulence approach.

11

Figure 4: Comparison of experimental and numerical predictions of turbulent kinetic energy for the Case B test case [51] at different locations of the domain, employing the standard $k - \epsilon$ model and the proposed ABL turbulence approach.
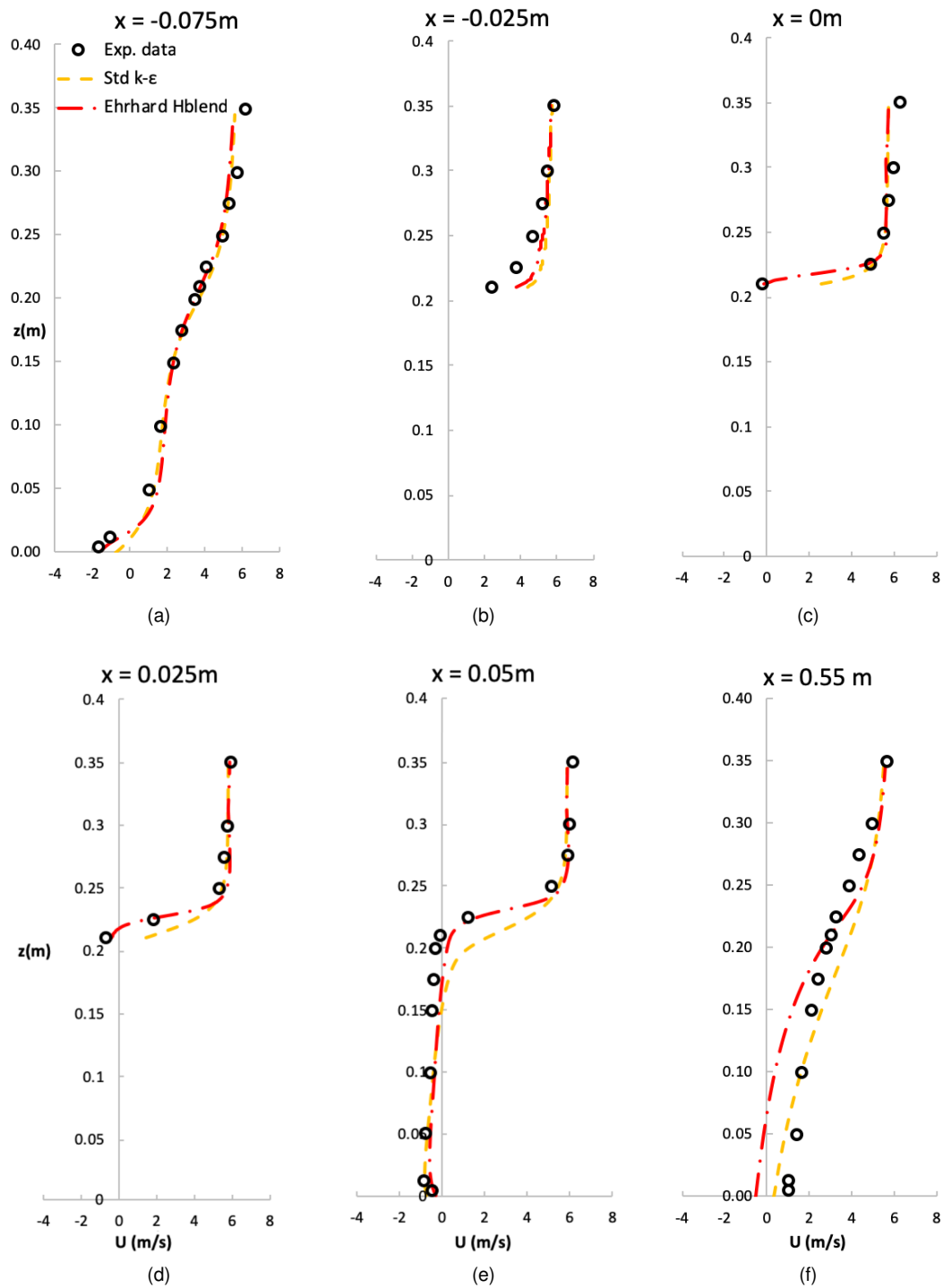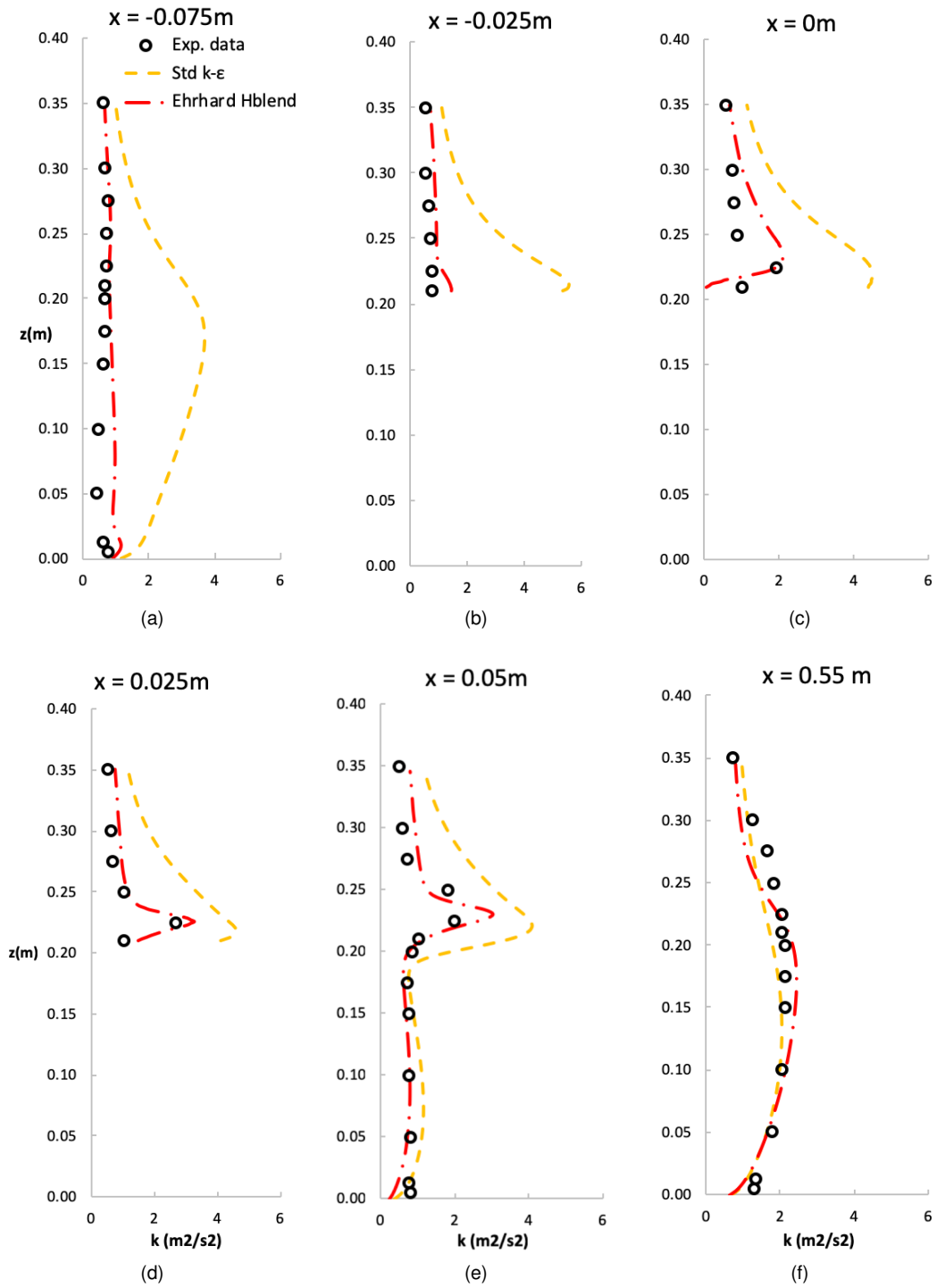
2.3. Urban Modelling Guidelines

Guidelines for domain sizing and mesh building can be found in Franke et al. [36, 52] and Tominaga et al.
[53]. The main guidelines considered for the current test-case are the following:

• Surroundings: buildings of height H_n have to be considered if they are within a distance of $6H_n$ from
the area of interest;

• Vertical extension: an extension of $5H_{max}$ above the tallest building is large enough to prevent artificial
acceleration of the flow;

• Extension in flow direction: outlet boundary is placed at a distance of $15H_{max}$ behind the last building.

In the purpose of this work, different wind directions were considered. Analogously to previous studies
[54, 55], the buildings of the Bovisa campus were rotated inside the domain when changing the flow direc-
tion, keeping the inflow plane perpendicular to the wind direction. To this end, all the sides were placed at
the maximum distance defined for the outlet.
In Figure 5a the zone of interest is marked with a yellow line, the blue circle is the centre of the domain and
a red triangle indicates the location of the target building. In Figures 5b and 5c, the CAD model and the
mesh extent are displayed to demonstrate the dimensions of the domain and the geometry considered.
The following step was the Wind Resource Assessment using experimental data recorded by an anemome-
ter placed in Bovisa Campus, and a further validation with a dataset provided by the Regional Environmental
Protection Agency (ARPA) [56]. Discrete directions were chosen with a step of $30°$, resulting in 12 simula-
tions, each with its proper inlet conditions.
A base-case was chosen to be analysed more in detail: the $270°$ (West to East) wind direction with an inlet
reference velocity of $5.82m/s$ at $17m$ of height. It was the most frequent wind direction, with almost 20%
relative frequency along the four years data records.
Once boundaries were defined, the mesh was built in OpenFOAM®. A first simulation was run to charac-
terize the target point for the turbine positioning, chosen to be above the impinging side of a structure on
the target building. A representation of the turbine positioning is shown in Figure 6.
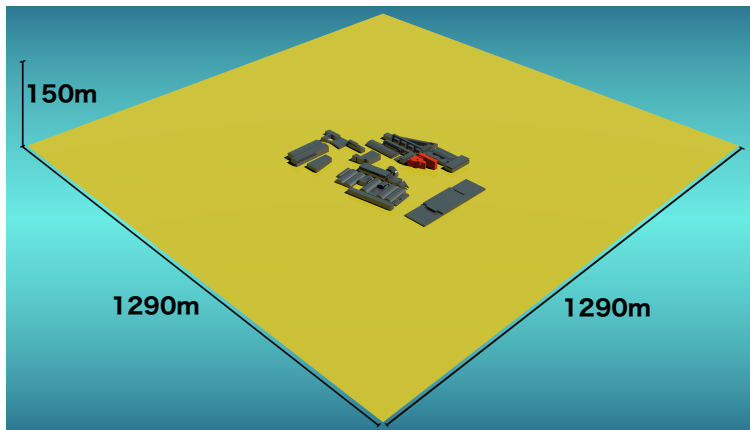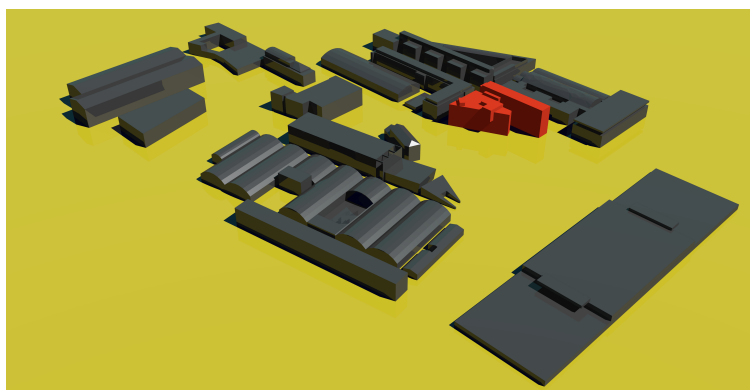
Figure 5: Zone of interest (Milan, Google Maps, 2019) (a), domain extent (b) and CAD model with the target building displayed in red (c) of the Bovisa campus.
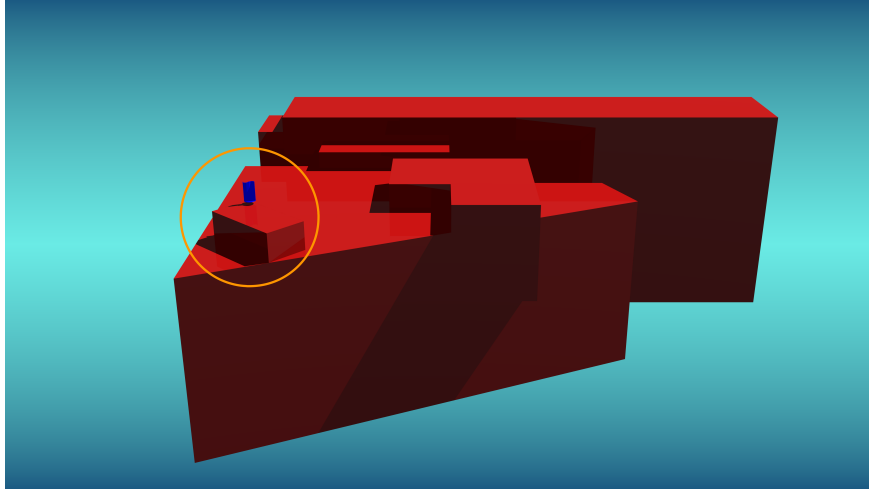
Figure 6: Turbine positioning on the target building.

2.4. Grid and GCI analysis

As for the grid distribution, the mesh is finest in the region of interest and close to the ground boundaries, then gradually decreasing in resolution. An approach with modular refinement using local boxes was used, with a local refinement for the region around the buildings and the highest level of refinement for the target building. This resulted in nearly 15 millions hexa cells. The grid distribution can be appreciated in Figure 7, for all the domain and for some strategic locations.

In the present work, two additional meshes were built, one coarser and one finer (refinement ratio $r = 1.45$), as shown in Table 3; the relative errors of wind velocity and TKE between Coarse-Medium and Medium-Fine meshes were computed in order to assess the non-dependence of the result from the grid refinement.

Table 3: Percentage error of U and k for the three differently refined meshes.

Refinement	Cells [Millions]	TKE % Error	U % Error
Coarse Mesh (f_3)	4,6	4%	2%
Medium Mesh (f_2)	15	5%	1.86%
Fine Mesh (f_1)	43	–	–

In addition, the GCI between refinement levels and convergence indexes for the two variables have been computed:

$$GCI = \frac{F_s \, |e|}{r^{p_c} - 1} \tag{4}$$

15
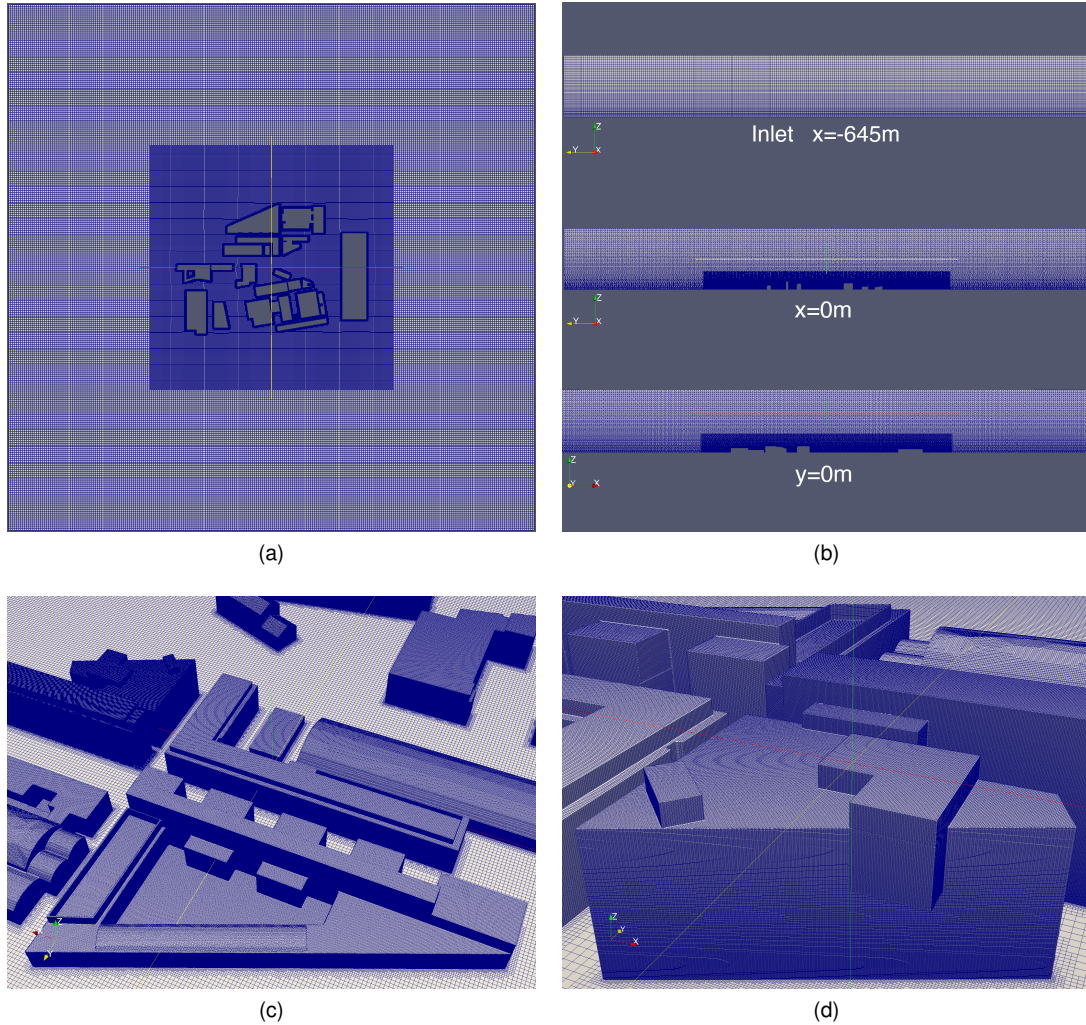
Figure 7: Computational mesh of the Bovisa campus on the domain ground (a), on the inlet and vertical $x = 0m$ and $y = 0m$ planes (b), on the buildings composing the campus (c) and on the target building (d).

where F_s is a safety factor: $F_s = 1.25$. The resulting GCIs are:

$$GCI_{12,TKE} = 2.7\% \qquad\qquad GCI_{23,TKE} = 0.7\% \qquad\qquad (5)$$

$$GCI_{12,U} = 3.2\% \qquad\qquad GCI_{23,U} = 1.81\% \qquad\qquad (6)$$

Due to the computational effort requested by the finest mesh, the medium one was chosen considering the limited discrepancy with the Fine mesh in terms of velocity and turbulent kinetic energy. Furthermore, the value of y⁺ is ranging from 40 to 350 around the buildings for the Medium mesh and from 30 to 270 for the Fine mesh, ensuring an appropriate level of refinement for the turbulence model.

16

3. Flow pattern around and over the target building

3.1. Methods and Algorithms

For the twelve wind directions, the inlet conditions from Table 1 were employed: u_* was determined using the available values of velocity for the considered wind direction. As for the k inlet profile, the coefficient C_1 and C_2 were retrieved through fitting to the semi-empirical relation of Brost and Wyngard [57]:

$$k\left(z\right) = \frac{1}{2}\left(\left\langle u'^2 \right\rangle + \left\langle v'^2 \right\rangle + \left\langle w'^2 \right\rangle\right) = \frac{u_*^2}{2}\left(8.7 - 6\frac{z}{h}\right) \tag{7}$$

where h is the ABL height. For neutral stratification conditions the value of h can be deduced from the following relation [58]:

$$\frac{hf_c}{u_*^2} \approx 0.33 \tag{8}$$

where a mid-latitude value for the Coriolis parameter, $f_c = 10^{-4} rad/s$, can be considered [59].

The operation for determining u_*, C_1 and C_2 was repeated per each wind direction considered. The area around the Bovisa campus is characterized by a topology consisting of decommissioned fields, few low-rise buildings, two extended railway junctions and a number of car parkings. Considering the reduced size of the urban roughness elements, z_0 was estimated to be equal to $0.4m$ [60, 61, 62].

Simulations were run in OpenFOAM®, employing the simpleFoam solver. Numerical schemes were set to second order, bounded for gradient and divergence with the help of specific limiters defined conveniently for the single terms. The geometric-algebraic multi-grid linear solver was employed for pressure, while the other variables were treated with smoothed linear solvers using Gauss-Seidel smoothers.

Convergence was assessed monitoring both residuals and the value of three variables using six probes positioned in different locations in the domain.

3.2. Base-Case Results

The aim of this Section is to extract the wind velocity distribution and use it as inlet condition to reliably simulate the behavior of the wind turbine: an incoming wind distribution that differs from the undisturbed or uniform profiles (namely the standard inlet profile used in wind turbines simulations), clearly represents a different operating condition for the machine.

To better interpret the level of disturbance of the flowfield around the buildings, the deviation parameter δ_h

17

212 is plotted in Figure 8a, at $5m$ of height. Whenever δ_h is equal to 0, the comprehensive approach is em-

213 ployed. A value close to 1 means that the flowfield is fully disturbed, leading to the application of the NLEV

214 model. A value between 0 and 1 distinguishes the transition zone. As expected, the highest values of BIA

215 are detected in correspondence of the wakes, the stagnation or deceleration zones generated by the urban

216 environment.

217 In Figure 8b, a contour plot of relative velocity is shown for a vertical plane intersecting the target building. It

218 can be observed that in proximity of the flat rooftops the fluid is accelerated with respect to the undisturbed

219 flowfield. The intersection with the sampling plane is indicated by a white arrow: here the acceleration due

220 to the presence of the obstacle itself was even more accentuated than in the upstream building, and the

221 relative velocity was higher than the one registered in the undisturbed flowfield at the same height.

222 Analogous results were obtained when running the base-case with the same turbulent settings and param-

223 eters on ANSYS Fluent R2019, whose relevant contour plots can be found in the supplementary material.
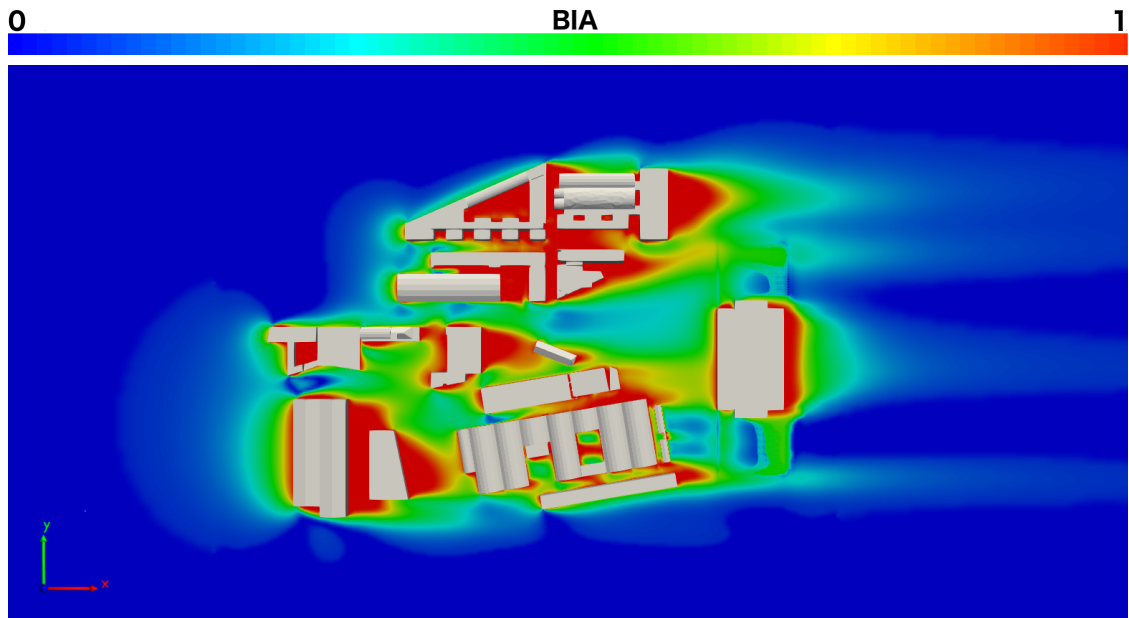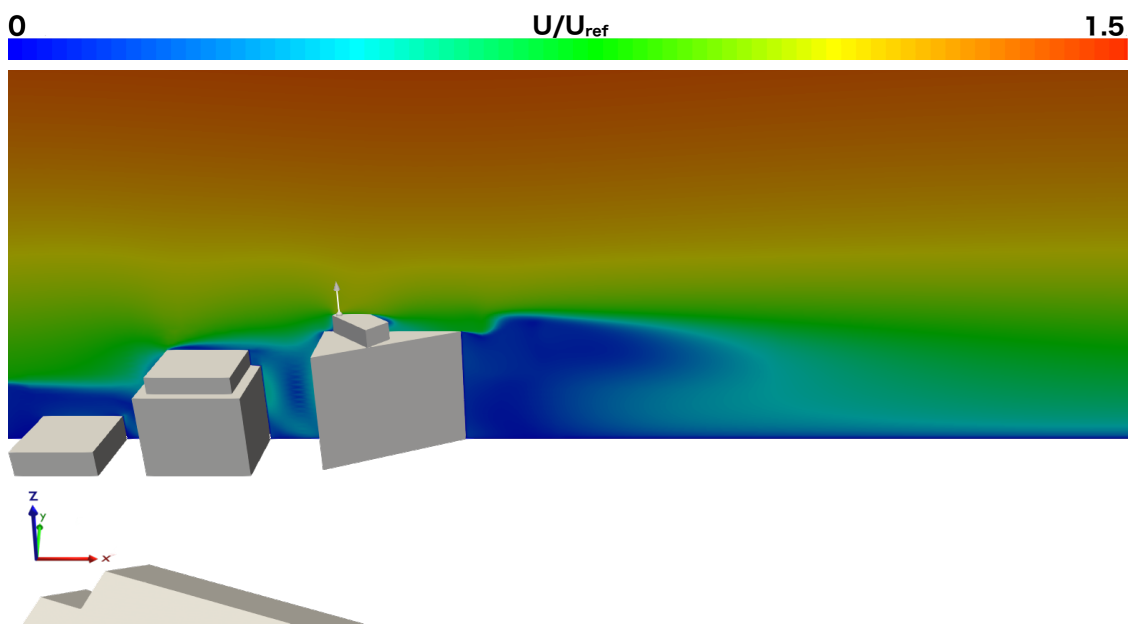
Figure 8: Contour plots of hybrid building influence area δ_h at the horizontal plane $z = 5m$ (a) and of relative velocity (U/U_R) in the vertical plane, over the target building (b), for the base-case simulation. The wind is flowing from left to right.

3.3. Sensitivity Analysis

In Figure 9 all the relative velocity samples for each wind direction are provided, preceded by a legend for direction and magnitude. The aim is to understand to which extent the obstacles affect the flow-stream when a specific wind direction is under study.

The sampling surface was rotated around the target point and was always perpendicular to the main wind direction.

The main results can be summarized as follows:

- in the $0°$, $30°$, $60°$ and $330°$ cases, the sample area on the target building was strongly influenced by the presence of the surrounding environment.

- the $120°$ and $150°$ cases presented a very large undisturbed area upstream the target building, which resulted as the only influence on the flow-stream.

- the remaining cases were influenced by low rising buildings that partially decelerated the stream-flow before it reached the target building.
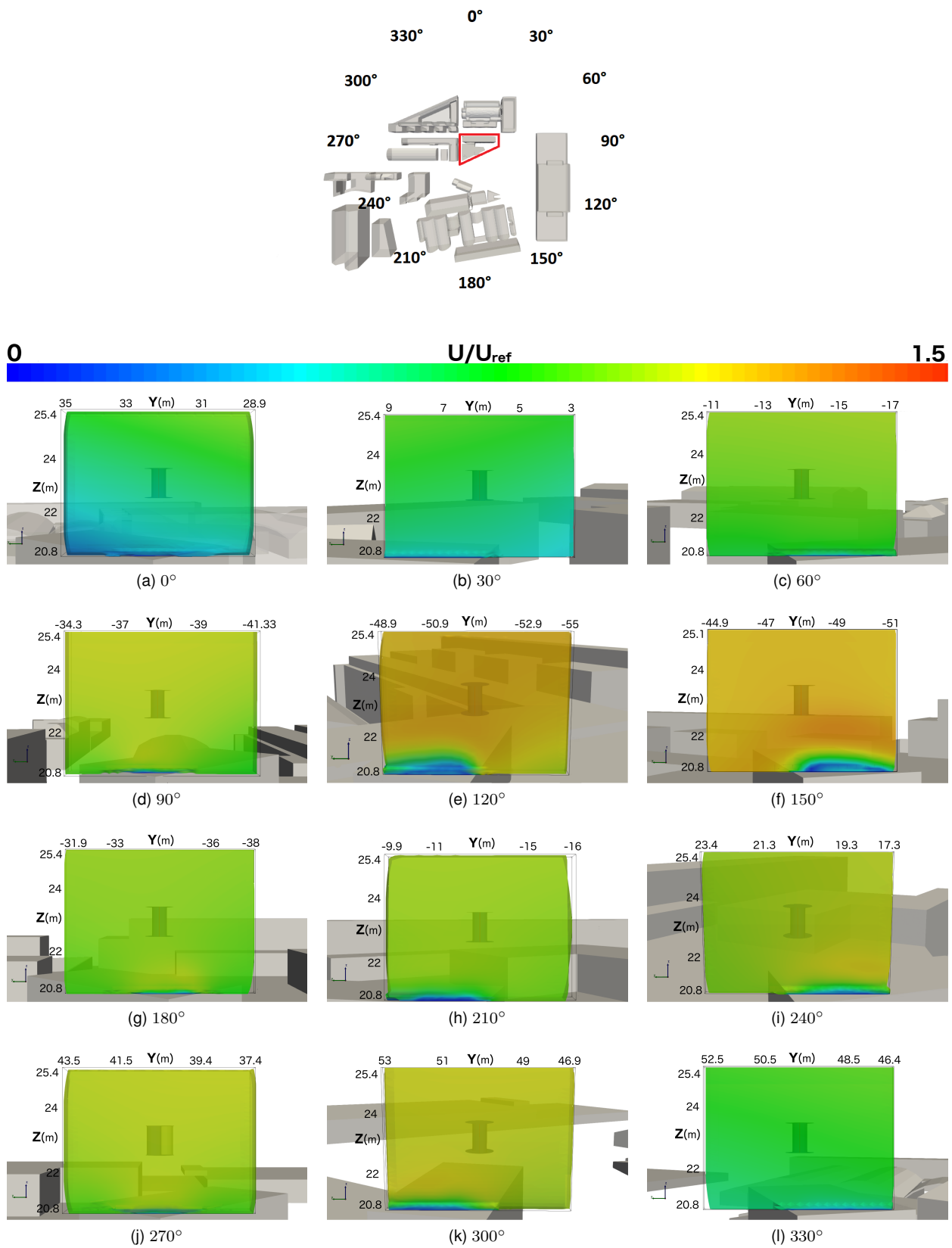
Figure 9: Normalized velocity U/U_{ref} distribution on sample surfaces perpendicular to the 12 considered wind directions.

3.4. Sampling for Turbine Simulations

The sampling of wind velocity distribution from the ABL mesh represents the link between meso (ABL) and micro (Turbine) spatial scales. The ABL mesh region around the target location has been further refined to reach the required resolution. Subsequently, the extracted wind velocity profiles were imposed as inlet conditions for the Turbine simulation session.

Sampling points were defined as follows: center point coordinates of the inlet surface of the Turbine mesh (about 1300 points) were extracted and moved upstream of the target point for turbine positioning. Sampled point data regarding velocity and turbulent characteristics were then used as inlet conditions for the turbine inlet surface and applied in the respective cell center points 8 meters upwind the Turbine position.

Two cases were selected for the turbine simulations: the $270°$ case, as it is the base-case of this work, and the $0°$ case, considering it was the most negatively affected by the surrounding obstacles.

In Figure 10a and 10b, the sample and the centreline plot of relative velocity are reported to highlight the increase of wind velocity magnitude at the turbine's height, in respect to the reference one. The velocity profile shows a gradient, that could affect the operating conditions and, consequently, the resulting efficiency of the machine. In particular, in the lower central area ($42m < y < 38m$ and $20.8m < z < 21.4m$), due to the presence of the roof, velocity tends to zero, while, above the aforementioned y limits, its value is not null. This contributes to create a longitudinal gradient, almost symmetrical with respect to the z axis.

Considering the $0°$ wind case, the sample and the centreline plot of relative velocity are displayed in Figures 11a and 11b. In this location the wind velocity magnitude is lower than the one in the reference case, for all the sample surfaces. Moreover, the velocity profile shows an even steeper gradient, varying along the surface, with higher slope from the left to the right side of the sample.

The results for the two wind conditions at $270°$ and $0°$ are used in the next Sections as inlet conditions for the turbine simulation. The performance of the turbine at ideal and real conditions, with disturbed flowfield, are compared to better understand the effect played by the urban environment on the potential energy production.

22
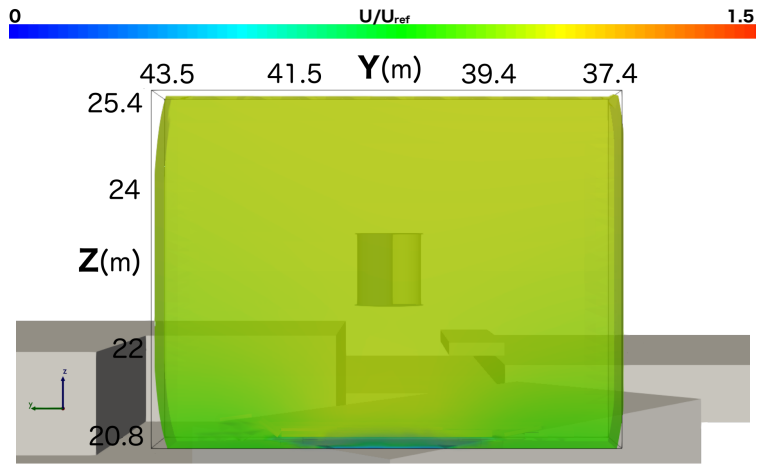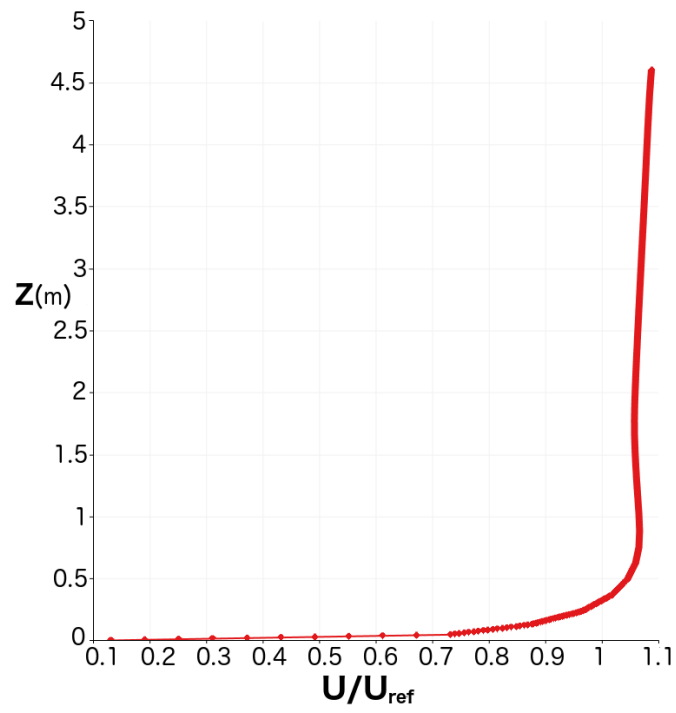
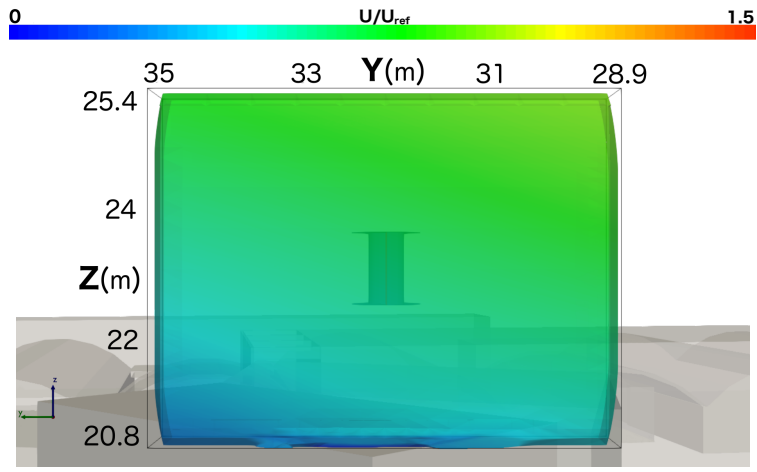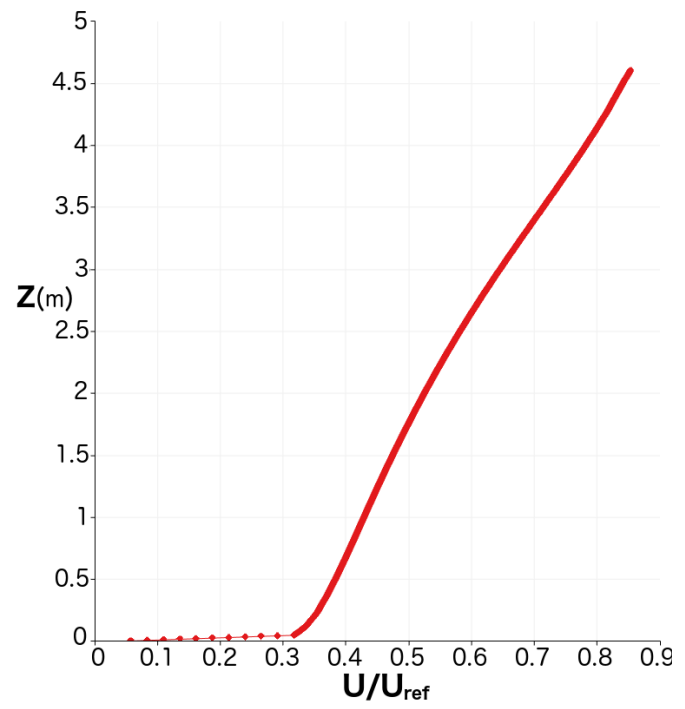Figure 10: Contour plot (a) and centreline profile (b) of dimensionless wind velocity for the $270°$ wind direction case.

Figure 11: Contour plot (a) and centreline profile (b) of dimensionless wind velocity for the $0°$ wind direction case.

4. Turbine Analysis

263 The model of the Savonius turbine, previously studied at ideal conditions by Ferrari et al. [28], is investi-

264 gated and the results compared with the ones obtained imposing the conditions for velocity and turbulent

265 quantities resulting from the ABL simulations.

4.1. Mesh and Turbulence Modelling

267 The model built by Ferrari et al. [28] is used in the present work, with the dimensions of the Sandia wind

268 tunnel [63]. The computational grid is shown in Figure 12, both in the vertical yz and horizontal xy planes.

The inlet is positioned at $x = -8m$ while the outlet at $x = 15m$ downstream. The lateral boundaries extend

(a)   (b)
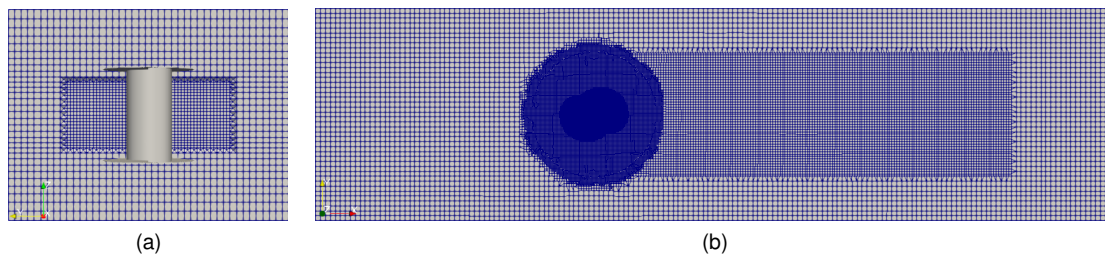
Figure 12: Computational mesh for the Savonius wind turbine, in the yz (a) and xy (b) planes.

269

270 for $6.1m$, with the turbine placed in the symmetry plane. The mesh employed in this study is the one

271 validated by Ferrari et al. [28] and Mereu et al. [29].

272 The choice of the turbulence model employed for this simulation is based on the sensitivity analysis of one

273 and two-equation RANS models performed by Nasef et al. [64] and Ferrari et al. [28], with the selection of

274 the SST $k - \omega$ model. The choice of a model based on the SST $k - \omega$ for the simulations of VAWTs was

275 recently suggested, also, by Rezaeiha et al. [65]. This closure solves the Wilcox's original $k - \omega$ model in

276 the near-wall region together with a transformed $k - \epsilon$ model in the far field, and blend them halfway [66].

277 As for the methods and algorithms, the same settings used in the previous work were employed [28, 29].

278 In particular, a transient solver for incompressible fluids on moving meshes was chosen, which uses the

279 PIMPLE algorithm, namely pimpleDyMFoam.

280 The results of Ferrari et al. [28] had already been validated with the experimental data of Blackwell [26].

281 Consequently mesh, numerical model and settings were considered reliable. For the purpose of this work,

282 the most relevant results were the values of power coefficient Cp, which indicates the efficiency of a wind

283 turbine.

25

284 From the comparison of the Cp trend of undisturbed (3D – CFD) and disturbed flows (Disturbed $0°$ and

285 $270°$) in Figure 13, it is evident the effect of the deviation of the velocity profiles, reported in Figure 10

286 (case $270°$) and Figure 11 (case $0°$). In particular, the flat profile with a value around $1.1U_{ref}$ for the case

287 $270°$ promotes the increase of Cp over the undisturbed case for higher TSR. The same influence can be

288 observed for the case at $0°$ that presents a velocity profile with a velocity ranging from 0.3 to $0.9U_{ref}$ and

shows a Cp trend similar to the undisturbed one, but with lower values for all the TSR investigated.
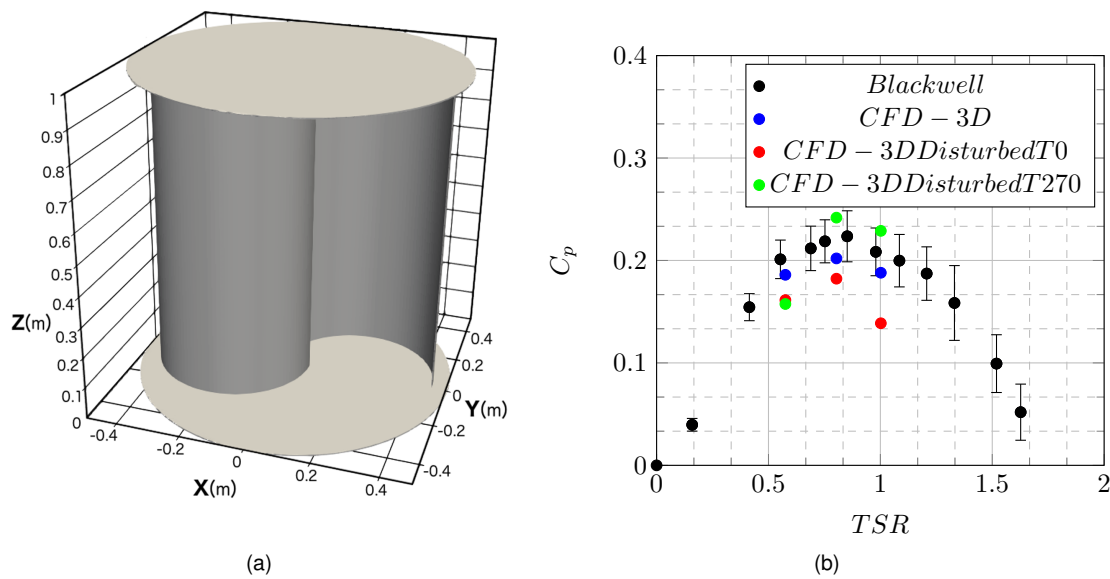
Figure 13: Savonius CAD model employed for the CFD simulation (a) and Cp obtained by 3D computational models and experimental data from Blackwell (b).

289

290 The reference-case for this part of the work is the optimal operating condition, at maximum efficiency (in

291 terms of power coefficient C_p), which was determined to be at $TSR = 0.81$.

292 A first trial simulation with an uniform inlet was run in order to compare the so-obtained results with the

293 cases under study. This first simulation was labelled as reference-case. For the $270°$ and $0°$ wind directions,

294 the rotational speed was changed to reach the same tip speed ratio of the reference-case, by imposing an

295 undisturbed velocity, turbulence characteristics of the flow in terms of turbulent kinetic energy k, its specific

296 dissipation rate ω and turbulent viscosity μ_t computed on the sampled points in projected area of the turbine.

4.2. Results

298 The different efficiency in the three cases is now discussed. Table 4 reports the force coefficients (torque

299 Cm, drag Cd, lift Cl), the power coefficient Cp and the error on Cp with respect to the reference-case.

26

Table 4: Force/power coefficients and error on power coefficient for the $270°$ and $0°$ wind cases.

	Cm	Cd	Cl	Cp	$\triangle$Cp
Reference-case	0.2686	1.0675	-0.9090	0.2176	
$270°$ **case**	0.2986	1.2854	-0.8096	0.2418	$+11\%$
$0°$ **case**	0.2250	1.1670	-0.8426	0.1822	-16%

The subsequent plots were re-scaled using the undisturbed velocity for each wind direction. Figure 14 shows a comparison of relative velocity in form of contour (at x coordinate $-1m$) and of plots over its centreline ($y = 0m$), between reference-case (dashed line) and $270°$ case (solid line). Dotted lines are provided for the $270°$ case at $y = 0.5m$ and $y = -0.5m$.

Figure 14: Comparison of relative velocity between the $270°$ case and the reference case at $x = -1m$ in the form of contour plots (a) and profiles (b). The red rectangle represents the area of interest.

Figure 14 shows that the presence of the turbine led to an analogous effect in both cases. However, in the zone of interest (red rectangle) the gradient of the sampled case was still evident and resulted in a higher relative velocity at the top section of the machine. At the bottom of the turbine the relative velocity seemed

27

307 to be almost equal in the two cases.

308 A further investigation on the reason behind Cp increase involved the analysis of the local Cm. The turbine

309 was subdivided in ten sections and local values of Cm were computed for both the current case and the

reference-case; for the sake of simplicity, only four sections were considered (Figure 15a).

(a)

(b)   (c)

Figure 15: Four selected sections of the Savonius wind turbine (a), with the corresponding polar chart of torque coefficients C_m for the $270°$ wind direction case (b) and the reference case (c).

310

311 From this analysis it followed that sections 1 to 3 had similar values of Cm, while the following sections

312 showed higher values. In particular, in the reference-case, sections 1 to 5 have the same Cm values of

313 the respective symmetrical sections 6 to 10; this behaviour was not observed in the sampled case. This

314 highlighted how the peculiar shape of the velocity profile had a relevant impact on the local performance on

28

315 each section.

316 Figure 16, through relative velocity contours and a centerline plot, compares the reference-case and the $0°$

case . The presence of a gradient of velocity is once again evident in the contour plots in Figure 16a.
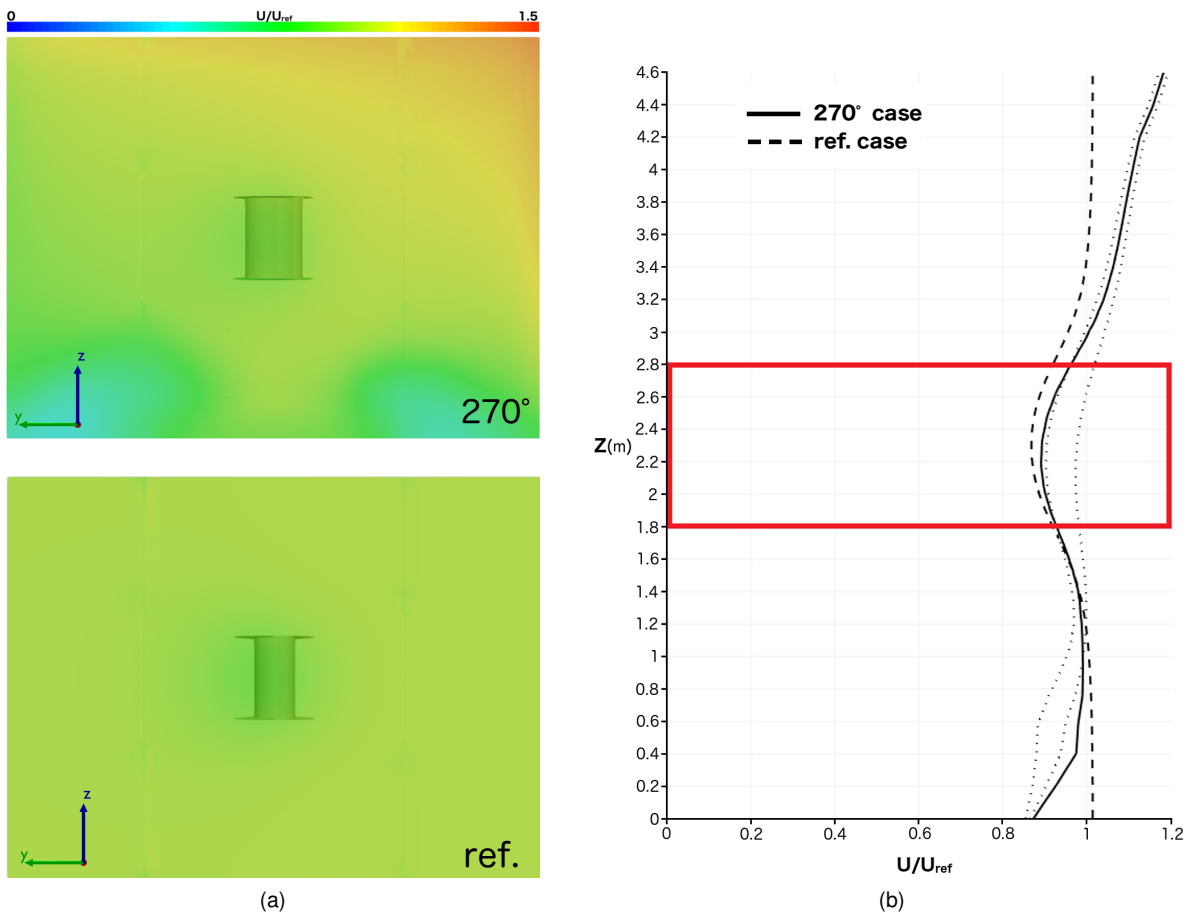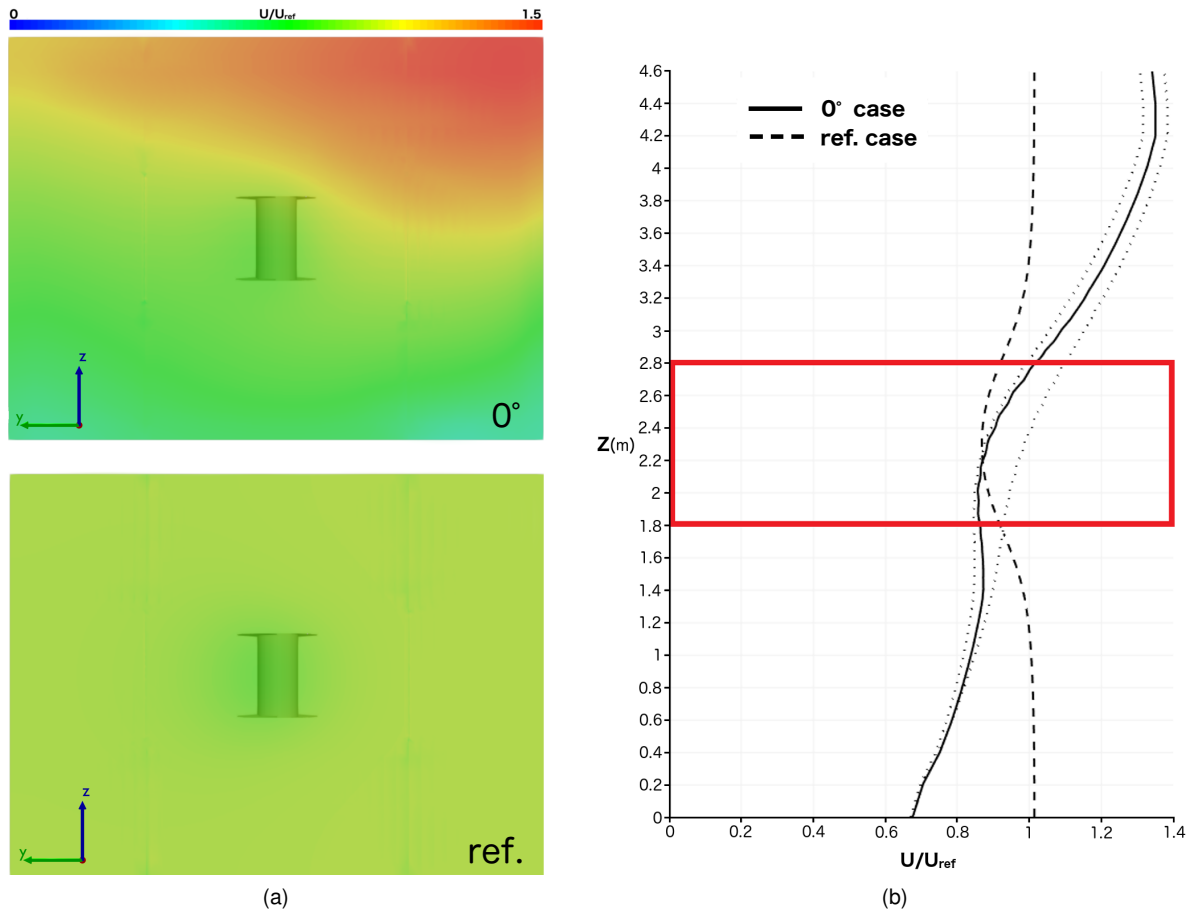

Figure 16: Comparison of relative velocity between the $0°$ case and the reference case at $x = -1m$ in the form of contour plots (a) and profiles (b). The red rectangle represents the area of interest.

317

318 Differently from the $270°$ case, the velocity profile showed an accentuated slope starting from the bottom of

319 the domain, leading to a low relative velocity at the turbine's lower plate.

320 The subdivision of the turbine in ten parts was applied, as previously done, in order to investigate local

321 values of Cm; the four chosen sections for this case are indicated in Figure 17a.

322 From a detailed analysis of these data it was deduced that, from sections 1 to 6, Cm values were lower than

323 the reference-case, while values from section 7 to 10 were higher, but still not enough to counter balance

324 the decreased section.
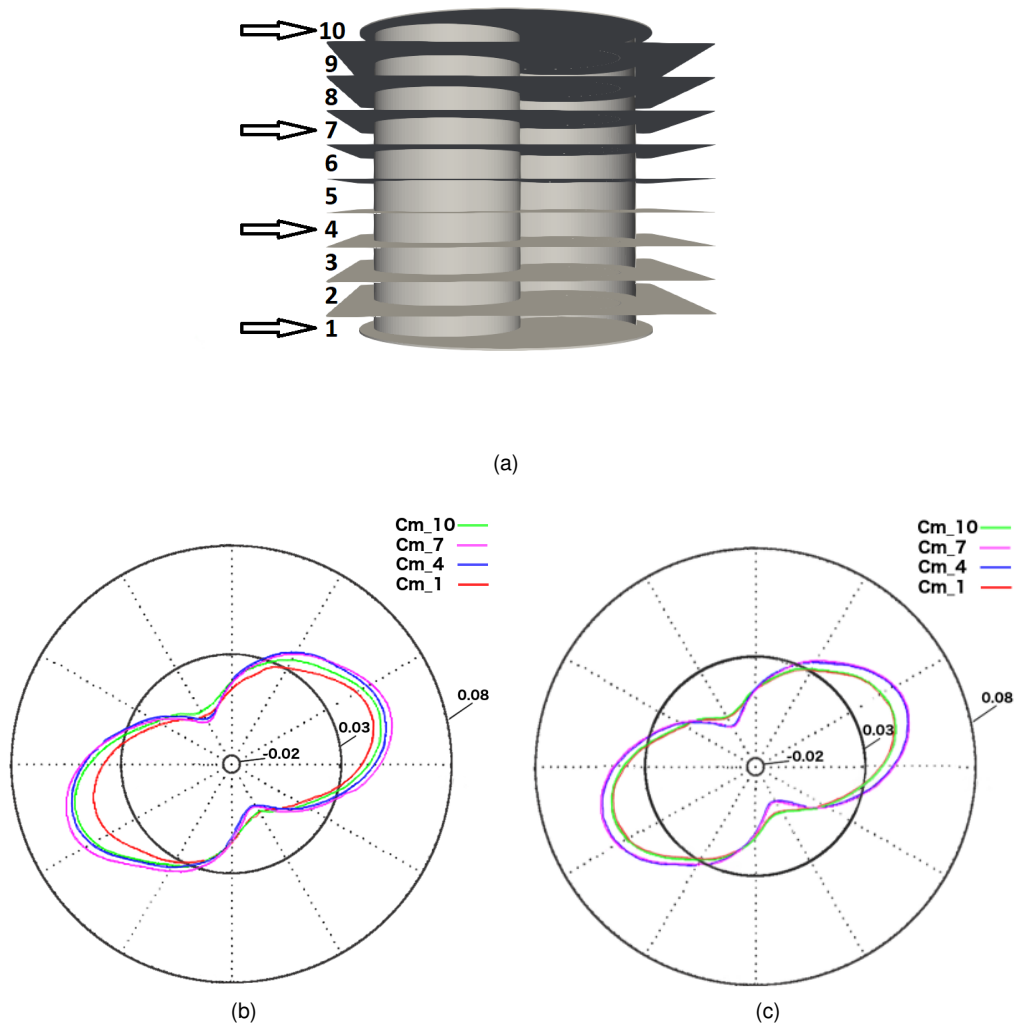
29
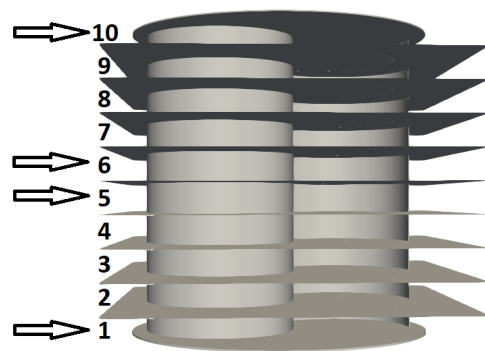
(a)
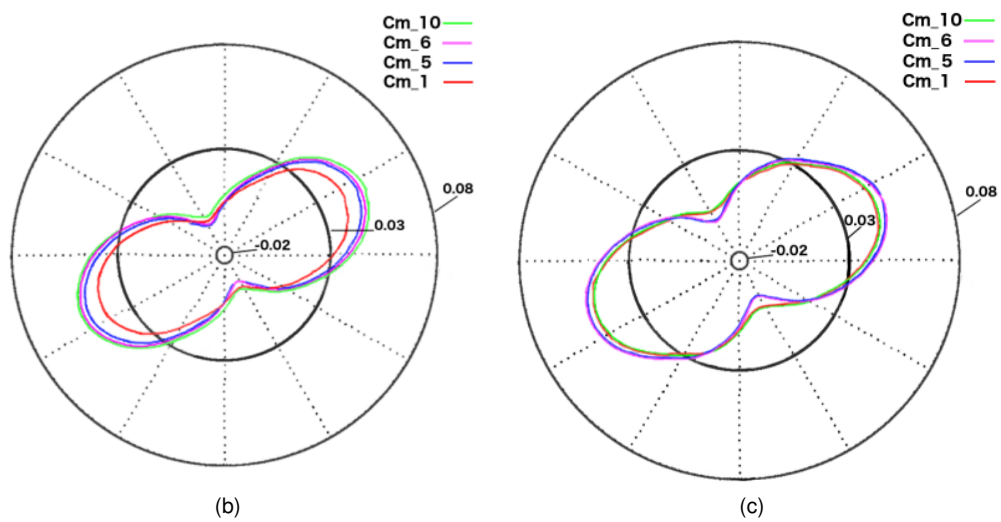
(b)

(c)

Figure 17: Four selected sections of the Savonius wind turbine (a), with the corresponding polar chart of torque coefficients C_m for the $0°$ wind direction case (b) and the reference case (c).

4.2.1. Energy Production

Finally, an analysis on the turbine's energy production was performed to assess if the variation of Cp led to a relevant difference on the machine's output. Samples for the different orientations were evaluated in relation to the previous analysis and two groups of cases were set up:

- Group1: wind directions from $90°$ to $300°$, whose relative velocity distribution on the centerline of the sampling face was very similar to the one of the $270°$ case; the Cp evaluated for the $270°$ case was assigned to this group.

- Group2: all wind directions involving near obstacles ($330°$, $0°$, $30°$, $60°$) whose velocity distribution resembled more the one of the $0°$ case; the Cp evaluated for the $0°$ case was assigned to this group.

The two groups have different impact on the result, due to the difference in both reference velocity (U_∞) and relative frequency (f_i) during the year. This led to a huge difference in the percentage of available power ($\%\mathrm{P}_{avail}$), as it can be seen in Table 5.

Table 5: Groups weight comparison on results.

	$\%\Delta$**Cp**	$\%$**P**$_{avail}$	$\%\Delta$ **E**
Group1	$+11\%$	97%	$+10.78\%$
Group2	-16%	3%	-0.55%

The case study showed a total increase of 10.23% on the annual energy yield with respect to the reference-case, due to the combination of the two groups of results.

To underline the importance of the first part of the present work (employment of ABL turbulence models for determining the flow pattern), the same study on energy yield was made also using the reference velocity derived from the Wind Resource Assessment.

If no wind simulations had been performed, the turbine performance would have been computed on the basis of those wind velocity values, with a uniform inlet profile at the turbine's inlet and the same value of Cp for all wind directions. This would have led to an underestimation of the annual energy yield of $11,53\%$ with respect to the reference-case with inlet velocity estimated at the sample surfaces, or to an underestimation of 19.74% with respect to the turbine simulations with sampled profiles.

Conclusions

This work stems from the awareness that district configuration severely impacts the exploitation of renewable energy, affecting the local wind conditions and the performance of a urban wind turbine. Considering the high variability of the urban environment, this effect is strongly case-dependent and hard to be parameterized. This further supports the deployment of computational fluid dynamics to comprehensively predict the flowfield in the area of interest.

The operating conditions of Savonius wind turbines should not be influenced by the horizontal change of wind direction. However, this is true only when ideal conditions and uniform inlet velocity distributions are involved. The deployment of CFD potential in this study has permitted to realistically predict the performance of the wind turbine under study, accounting for all the elements disturbing the flowfield. Without this analysis, all these observations could have been made only after the installation of the machine, leading, at least, to erroneous prediction in productivity or to inadequate positioning of the wind turbine. For this reason, this study suggests that even for small scale production with building integrated wind farms, a wind simulation campaign accounting for the local ABL and orography features should be employed to quantify the effective availability of wind resource and to optimize investments in urban-wind renewable source exploitation.

Future improvements to the wind resource assessment could include the deployment of urban sensors for optimal data assimilation, as suggested by Sousa et al. [67], and the performing of wind gallery experiments to further assess the reliability of the numerical results.

References

[1] D. Mauree, E. Naboni, S. Coccolo, A.T.D. Perera, V. M. Nik, and J. Scartezzini. A review of assessment methods for the urban environment and its energy sustainability to guarantee climate adaptation of future cities. *Renewable and Sustainable Energy Reviews*, 112:733–746, 2019.

[2] G. Al Zohbi, P. Hendrick, and Ph. Bouillard. Evaluation of the impact of wind farms on birds: The case study of lebanon. *Renewable Energy*, (80):682–689, 2015.

[3] R. Mamani, N. Hackenberg, and P. Hendrick. Efficiency of high altitude on-shore wind turbines: Air density and turbulence effects—qollpana wind farm (bolivia). *proceedings*, (2(8)):487, 2018.

[4] A. Morabito and P. Hendrick. Pump as turbine applied to micro energy storage and smart water grids: A case study. *Applied Energy*, (241):557–579, 2019.

[5] G. de Oliveira e Silva and P. Hendrick. Pumped hydro energy storage in buildings. *Applied Energy*, (179):1242–1250, 2016.

[6] S. Giorgetti, G. Pellegrini, and G. Zanforlin. Cfd investigation on the aerodynamic interferences between medium-solidity darrieus vertical axis windturbines. *Energy Procedia*, (81):227–239, 2015.

[7] K. Kacprzak, G. Liskiewicz, and K. Sobczak. Numerical investigation of conventional and modified savonius wind turbines. *Renewable Energy*, (60):578–585, 2013.

[8] H. L. Bai, C. M. Chan, X. M. Zhu, and K. M. Li. A numerical study on the performance of a savonius-type vertical-axis wind turbine in a confined long channel. *Renewable Energy*, (139):102–109, 2019.

[9] J. Sousa and C. Gorlé. Computational urban flow predictions with bayesian inference: Validation with field data. *Building and Environment*, 154:13–22, 2019.

[10] F. Toja-Silva, T. Kono, C. Peralta, O. Lopez-Garcia, and J. Chen. A review of computational fluid dynamics (cfd) simulations of the wind flow around buildings for urban wind energy exploitation. *Journal of Wind Engineering and Industrial Aerodynamics*, (180):66–87, 2018.

[11] C. G. Sánchez, J. van Beeck, and C. Gorlé. Predictive large eddy simulations for urban flows: Challenges and opportunities. *Building and Environment*, 139:146–150, 2018.

[12] O. Temel and J. van Beeck. Two-equation eddy viscosity models based on the monin–obukhov similarity theory. *Applied Mathematical Modelling*, (42):1–16, 2017.

[13] O. Temel, S. Porchetta, and J. Bricteux, L. van Beeck. Rans closures for non-neutral microscale cfd simulations sustained with inflow conditions acquired from mesoscale simulations. *Applied Mathematical Modelling*, (53):635–652, 2018.

[14] P. Richards and R. Hoxey. Appropriate boundary conditions for computational wind engineering models using the k–epsilon turbulence model. *Journal of Wind Engineering and Industrial Aerodynamics*, (46(47)):145–153, 1993.

[15] A. Parente and C. Benocci. On the rans simulation of neutral abl flows. 2010.

[16] R. Longo, M. Ferrarotti, C. Garcia Sanchez, M. Derudi, and A. Parente. Advanced turbulence models and boundary conditions for flows around different configurations of ground-mounted buildings. *Journal of Wind Engineering and Industrial Aerodynamics*, (167):160–182, 2017.

[17] R. Longo, M. Fürst, , M. Ferrarotti, M. Deurdi, and A. Parente. Cfd dispersion study based on a variable schmidt formulation for flows around different configurations of ground-mounted buildings. *Building and Environment*, 154:336–347, 2019.

[18] A. Parente, C. Gorlè, J. van Beeck, and C. Benocci. Improved k–e model and wall function formulation for the rans simulation of abl flows. *Journal of Wind Engineering and Industrial Aerodynamics*, (99):267–278, 2011.

33

[19] M. Pontiggia, M. Derudi, V. Busini, and R. Rota. Hazardous gas dispersion: A cfd model accounting for atmospheric stability classes. *Journal of Hazardous Materials*, 171(1 - 3):739 – 747, 2009.

[20] F.S. Lien, W.L. Chen, and M.A. Leschziner. Low reynolds-number eddy-viscosity modelling based on non-linear stress-strain/vorticity relations. *Engineering Turbulence Modelling and Experiments 3*, 1996.

[21] T. J. Craft, B. E. Launder, and K. Suga. Development and application of a cubic eddyviscosity model of turbulence. *International Journal of Heat and Fluid Flow*, 17:108–115, 1995.

[22] J. Ehrhard and N. Moussiopoulos. On a new non-linear turbulence model for simulating flows around building shaped structures. *Journal of Wind Engineering and Industrial Aerodynamics*, (88):91–99, 2000.

[23] A. Parente, C. Gorlè, J. van Beek, and C. Benocci. A comprehensive modelling approach for the neutral atmospheric boundary layer (abl): Consistent inflow conditions, wall function and turbulence model. *Boundary-Layer Meteorology*, 2011.

[24] W. Tian, Z. Mao, B. Zhang, and Y. Li. Shape optimization of a savonius wind rotor with different convex and concave sides. *Renewable Energy*, (117):287–299, 2018.

[25] A. Vergaerde, T. De Troyer, L. Standaert, J. Kluczewska-Bordier, A. Pitance, A. Immas, F. Silvert, and M. C. Runacres. Experimental validation of the power enhancement of a pair of vertical-axis wind turbines. *Renewable Energy*, (146):181–187, 2020.

[26] B.F. Blackwell, R.E. Sheldahl, and L.V. Feltz. *Wind Tunnel Performance Data for Two- and Three-Bucket Savonius Rotor*. 1977.

[27] N.H. Mahmoud, A.A. El-Haroun, E. Wahba, and M.H. Nasef. An experimental study on improvement of savonius rotor performance. *Alexandria Engineering Journal*, (51):19–25, 2012.

[28] G. Ferrari, D. Federici, P. Schito, F. Inzoli, and R. Mereu. Cfd study of savonius wind turbine: 3d model validation and parametric analysis. *Renewable Energy*, 105:722–734, 2017.

[29] R. Mereu, D. Federici, G. Ferrari, P. Schito, and F. Inzoli. Parametric numerical study of savonius wind turbine interaction in a linear array. *Renewable Energy*, 113:1320–1332, 2017.

[30] E. Antar and M. Elkhoury. Parametric sizing optimization process of a casing for a savonius vertical axis wind turbine. *Renewable Energy*, (136):127–138, 2019.

[31] L. Sumei, P. Wuxuan, Z. Xingwang, Z. Hao, C. Xionglei, L. Zhengwei, and C. Qingyan. *Influence of surrounding buildings on wind flow around a building predicted by CFD simulations*. Number 140. 2018.

[32] J. Srebric, M. Heidarinejad, and j. Liu. Building neighborhood emerging properties and their impacts on multi-scale modeling of building energy and airflows. *Building and Environment*, (91):246–262, 2015.

[33] A. L. Pisello, J. E. Taylor, X. Xu, and F Cotana. Inter-building effect: Simulating the impact of a network of buildings on the accuracy of building energy performance predictions. *Building and Environment*, (58):37–45, 2012.

[34] K. C. Anup, J. Whale, and T. Urmee. Urban wind conditions and small wind turbines in the built environment: A review. *Renewable Energy*, (113):268–283, 2019.

[35] T. Sharpe and G. Proven. Crossflex: Concept and early development of a true building integrated wind turbine. *Energy and Buildings*, (42):2365–2375, 2010.

[36] J. Franke, A. Hellsten, H. Schlunzen, and B. Carissimo. *Best Practice Guideline for the CFD Simulation Of Flows in the Urban Environment*. University of Hamburg Centre of Marine and Atmospheric Sciences, 2007.

[37] M. Pontiggia, G. Landucci, V. Busini, M. Derudi, M. Alba, M. Scaioni, S. Bonvicini, V. Cozzani, and R. Rota. Cfd model simulation of lpg dispersion in urban areas. *Atmospheric Environment*, 45:3913–3923, 2011.

[38] V. Busini and R. Rota. Influence of the shape of mitigation barriers on heavy gas dispersion. *Journal of Loss Prevention in the*

443 *Process Industries*, 29:13–21, 2014.

[39] P. Ouro, B. Fraga, N. Viti, A. Angeloudis, T. Stoesser, and C. Gualtieri. Instantaneous transport of a passive scalar in a turbulent separated flow. *Environmental Fluid Mechanics*, 2017.

[40] H.K. Versteeg and W. Malalasekera. *An introduction to computational fluid dynamics - the finite volume method*. Pearson, 2007.

[41] W. Bauer, W. Haag, and D.K. Hennecke. Accuracy and robustness of nonlinear eddy viscosity models. *International Journal of Heat and Fluid Flow*, 21:312–319, 2000.

[42] H.G. Kim, V.C Patel, and C.M. Lee. Numerical simulation of wind flow over hilly terrain. *Journal of Wind Engineering and Industrial Aerodynamics*, 87:45–60, 2000.

[43] K.W. Ayotte, D. Xu, and P. A. Taylor. The impact of turbulence closure schemes on predictions of the mixed spectral finite-difference model for flow over topography. *Boundary-Layer Meteorology*, 68:1–33, 1994.

[44] M. Balogh, A. Parente, and C. Benocci. Rans simulation of abl flow over complex terrains applying an enhanced k-ϵ model and wall function formulation: Implementation and comparison for fluent and openfoam. *Journal of Wind Engineering and Industrial Aerodynamics*, (104-106):360–368, 2012.

[45] A. Parente, R. Longo, and M. Ferrarotti. *CFD boundary conditions, turbulence models and dispersion study for flows around obstacles*. VKI LS 2017-01, 2017.

[46] A. Parente, R. Longo, and M. Ferrarotti. *Turbulence model formulation and dispersion modelling for the CFD simulation of flows around obstacles and on complex terrains*. VKI LS 2019-03, 2019.

[47] R. Longo, , Marco Ferrarotti, and A. Parente. Cubic turbulence closures and dispersion models for flows around different configurations of ground-mounted buildings. ETMM11 - 11th International ERCOFTAC Symposium on Engineering Turbulence Modelling and Measurements, 2016.

[48] R. Longo, A. Bellemans, M. Ferrarotti, M. Derudi, and A. Parente. A new turbulent schmidt number formulation based on the local turbulence level. *ETMM12 - 12th International ERCOFTAC Symposium on Engineering Turbulence Modelling and Measurements*, 2018.

[49] C. Peralta, A. Parente, M. Balogh, and C. Benocci. Rans simulation of the atmospheric boundary layer over complex terrain with a consistent k-epsilon model formulation. *Proceedings of the 6th International Symposium on Computational Wind Engineering (CWE2014)*, (Hamburg, Germany):236–237, 2014.

[50] H. Montazeri and B. Blocken. Cfd simulation of wind-induced pressure coefficients on buildings with and without balconies: Validation and sensitivity analysis. *Building and Environment*, 60:137–149, 2013.

[51] Y. Tominaga, A. Mochida, T. Shirasawa, R. Yoshie, H. Kataoka, K. Harimoto, and T. Nozu. Cross comparisons of cfd results of wind environment at pedestrian level around a high-rise building and within a building complex. page 257–266. Journal of Asian Architecture and Building Engineering, 2004.

[52] J. Franke, C. Hirsh, A. Jensen, H. Krus, M. Schatzmann, P. Westbury, S. Miles, J. Wisse, and N. Wright. *Reccomandations on the Use of CFD in Wind Engineering*. University of Hamburg Centre of Marine and Atmospheric Sciences, 2004.

[53] Y. Tominaga, A. Mochida, R. Yoshie, H. Karaoka, T. Nozu, Y. Masaru, and T. Shirasawa. Aij guidelines for practical applications of cfd to pedestrian wind environment around buildings. *Journal of Wind Engineering and Industrial Aerodynamics*, (96):1749–1761, 2008.

[54] C. Gorlè, ClaraGarcia-Sanchez, and G. Iaccarino. Quantifying inflow and rans turbulence model form uncertainties for wind engineering flows. *Journal of Wind Engineering and Industrial Aerodynamics*, (144):202–212, 2015.

[55] C. García-Sánchez, D. A. Philips, and C. Gorlé. Quantifying inflow uncertainties for cfd simulations of the flow in downtown

oklahoma city. *Building and Environment*, (78):118–129, 2014.

[56] ARPA. Regional environmental protection agency, 2019.

[57] R. A. Brost and J. C. Wyngaard. A model study of the stably stratified planetary boundary layer. *Journal of the Atmospheric Sciences*, 35(8):1427–1440, 1978.

[58] A Bechmann. *Large-Eddy Simulation of Atmospheric Flow over Complex Terrain*. PhD thesis, Technical University of Denmark, 2006.

[59] A. Parente and M. Longo, R. Ferrarotti. *CFD boundary conditions, turbulence models and dispersion study for flows around obstacles*, volume CFD for atmospheric flows and wind engineering - hardcover - VKI LS 2017-01. 2017.

[60] S. Liu, W. Pan, H. Zhang, X. Cheng, Z. Long, and Q. Chenm. Cfd simulations of wind distribution in an urban community with a full-scale geometrical model. *Building and Environment*, (117):11–23, 2017.

[61] B. Blocken, T Stathopoulos, and J. Carmeliet. Cfd simulation of the atmospheric boundary layer: wall function problems. *Atmospheric Environment*, (41):238–252, 2007.

[62] J. Wieringa. Updating the davenport roughness classification. *Wind Eng. Ind. Aerodyn.*, (41):357–368, 1992.

[63] B. Blackwell, R. Sheldahl, and L. Feltz. Wind tunnel performance data for two and three bucket savonius rotors. *J. Energy*, pages 160–164, 1977.

[64] M. Nasef, W. El-Askary, H. Abdel-Hamid, and H. Gad. Evaluation of savonius rotor performance: static and dynamic studies. *J. Wind Eng. Ind. Aerodyn.*, (123):1–11, 2013.

[65] A. Rezaeiha, H. Montazeri, and B. Blocken. On the accuracy of turbulence models for cfd simulations of vertical axis wind turbines. *Energy*, 180:838–857, 2019.

[66] F.R. Menter. Zonal two equation k-omega turbulence models for aerodynamic flows. *24th Fluid Dynamics Conference*, 1993.

[67] J. Sousa, C. G. Sánchez, and C. Gorlé. Improving urban flow predictions through data assimilation. *Building and Environment*, 132:282–290, 2018.